

Inter- to intra-layer resistivity anisotropy of NdFeAs(O,H) with various hydrogen concentrations

M. Y. Chen ¹, K. Iida ^{1,3}, K. Kondo,¹ J. Hänisch ², T. Hatano,^{1,3} and H. Ikuta ¹¹Department of Materials Physics, Nagoya University, Nagoya 464-8603, Japan²Institute for Technical Physics, Karlsruhe Institute of Technology, Hermann-von-Helmholtz-Platz 1, 76344 Eggenstein-Leopoldshafen, Germany³JST CREST, Kawaguchi, Saitama 332-0012, Japan

(Received 30 December 2021; accepted 1 April 2022; published 2 May 2022)

With molecular beam epitaxy and a topotactic chemical reaction, we prepared NdFeAs(O,H) epitaxial thin films with various hydrogen concentrations on 5° vicinal-cut MgO substrates. By measuring the resistivities along the longitudinal and transversal directions, the *ab*-plane and the *c*-axis resistivities (ρ_{ab} and ρ_c) were obtained. The resistivity anisotropy $\gamma_\rho \equiv \rho_c/\rho_{ab}$ of NdFeAs(O,H) with various hydrogen concentrations was compared with that of NdFeAs(O,F). At the H concentrations which led to superconducting transition temperatures T_c over 40 K, γ_ρ recorded ~ 100 – 150 at 50 K. On the other hand, a low γ_ρ value of 9 was observed with the highest-doped sample. The exponent β of the *ab*-plane resistivity obtained by fitting a power-law expression $\rho_{ab}(T) = \rho_0 + AT^\beta$ to the data was close to unity down to a low temperature in the vicinity where the second antiferromagnetic phase locates, which may be related to the quantum critical point discussed at the overdoped side of the phase diagram.

DOI: [10.1103/PhysRevMaterials.6.054802](https://doi.org/10.1103/PhysRevMaterials.6.054802)

I. INTRODUCTION

Mixed-anion compounds have recently been attracting considerable attention since they are rich in emergent phenomena, e.g., acid nitride photocatalysts [1] and acid hydride proton conductors [2]. The iron-based mixed-anion compound *Ln*FeAsO (*Ln* = Nd and Sm) shows superconductivity with a maximum transition temperature T_c of 56 K when oxygen is partially substituted by fluorine (*Ln*FeAsO_{1-x}F_x) or hydrogen (*Ln*FeAsO_{1-x}H_x) [3–5]. These substitutions lead to electron doping ($O^{2-} \rightarrow H^-/F^- + e^-$), therefore, the carrier concentration is determined by the amount of F or H. The decisive difference between fluorine and hydrogen is the solubility limit: The latter can be substituted up to $x \sim 0.8$ [6], whereas the former about $x = 0.2$ at ambient pressure [7].

*Ln*FeAsO crystalizes in a laminated structure with alternating *Ln*O charge reservoirs and FeAs conduction layers along the *c*-axis direction. Therefore, the electromagnetic properties of *Ln*FeAsO are anisotropic. From the viewpoint of application a low electromagnetic anisotropy is favorable. Compared with F-doped *Ln*FeAsO, hydrogen-substituted *Ln*FeAsO has a more three-dimensional Fermi surface, and, thus, a lower anisotropy can be expected [8]. Additionally, the character of the Fermi surface may depend on the carrier doping level as was shown for another Fe-based superconductor, BaFe₂As₂ [9,10]. Hence, it is interesting to explore how the electromagnetic anisotropy of *Ln*FeAsO_{1-x}H_x changes as a function of doping level.

The resistivity anisotropy γ_ρ , defined as the ratio ρ_c/ρ_{ab} where ρ_c and ρ_{ab} are the out-of-plane and in-plane resistivities, is related to the mass anisotropy $\gamma_m \equiv m_c/m_{ab}$ where m_c and m_{ab} are the out-of-plane and in-plane effective masses,

respectively. Polycrystalline *Ln*FeAsO samples with different hydrogen contents have been used for exploring physical quantities [11], but they are not ideal platforms for investigating the electromagnetic anisotropy. Unfortunately though, fabrication of sufficiently large H-doped *Ln*FeAsO single crystals seems to be still difficult, and only a few studies have been reported measuring the resistivity anisotropy of doped *Ln*FeAsO [12–15]. Recently, SmFeAsO_{0.9}H_{0.1} single crystals have been grown by combining a Na₃As flux and a high-pressure synthesis method [15]. The γ_ρ of the resultant crystals increased from ~ 3 at 300 K to 8 at 50 K. However, it is not clear how the resistivity anisotropy depends on the hydrogen content, in particular at high concentration.

Recently, hydrogen-doped *Ln*FeAsO epitaxial thin films have been fabricated via a topotactic chemical reaction [16–18]. In one of these works, we showed that hydrogen contents can be varied by controlling the processing temperature T_{proc} [18], which enables us to investigate the physical quantities as a function of carrier concentration. Additionally, we have successfully grown off-axis NdFeAsO thin films using vicinal substrates in an earlier work [19] from which the out-of-plane resistivity can be extracted. Combining these two methods, NdFeAs(O,H) thin films having different H concentrations were grown on vicinal-cut MgO substrates in the present paper. We measured the transport properties of these films and discussed how the physical quantities and their anisotropy depend on the carrier concentration.

II. EXPERIMENT

The parent NdFeAsO thin films with thicknesses of 20–30 nm were grown by molecular beam epitaxy (MBE) at 800 °C.

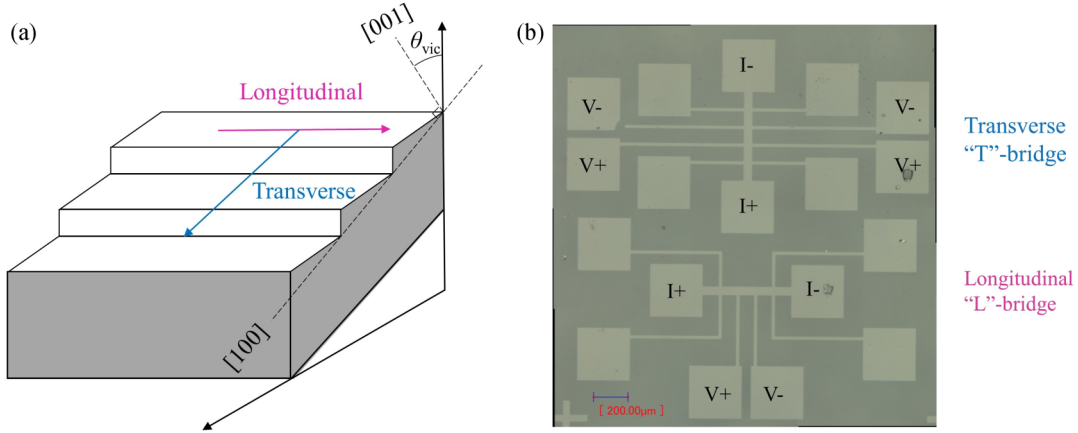


FIG. 1. (a) Schematic of a vicinal-cut substrate. The [001] axis is tilted from the direction normal to the substrate surface by θ_{vic} . (b) An example of a top-view optical micrograph of the microbridges. A bridge running along the transverse direction is labeled as a T bridge, whereas a bridge perpendicular to the transverse direction is labeled as an L bridge.

Fe, As, NdF_3 , Fe_2O_3 , and Ga were charged in Knudsen cells. Here, oxygen was supplied via the thermal decomposition of Fe_2O_3 , whereas Ga was used to remove F according to $\text{NdF}_3 + \text{Ga} \rightarrow \text{Nd} + \text{GaF}_3$. The growth procedure was described in detail in Ref. [20]. The film growth was monitored *in situ* by reflection high-energy electron diffraction. Instead of normal $\text{MgO}(001)$ substrates, $5 \times 10 \text{ mm}^2$ -sized vicinal-cut substrates with the [001] axis inclined by $\sim 5^\circ$ with respect to the direction normal to the surface were used for extracting the out-of-plane resistivity [Fig. 1(a)]. After the film growth, x-ray diffraction (XRD) analysis was performed: $2\theta/\omega$ scans were used for evaluating the phase purity and the c -axis lattice parameter. Because the film grows with an offset angle on a vicinal-cut substrate, we also conducted ω scans with the angle 2θ fixed to the 003 reflection of NdFeAsO to determine the offset angle α precisely. The angle ω that maximizes the diffraction intensity corresponds to α .

Doping hydrogen into NdFeAsO was conducted similarly to Ref. [18]. As-grown films were cut into smaller samples having a size of $5 \times 5 \text{ mm}^2$. The sample was placed in an Al_2O_3 crucible filled with CaH_2 powder ($\sim 0.8 \text{ g}$) as hydrogen source. The whole arrangement was placed in a quartz tube (outer diameter 12 mm and length 150 mm) and then sealed under vacuum. Importantly, the surface of the film had to be physically in contact with the CaH_2 powder. Then the quartz tube was heated to $T_{\text{proc}} = 440\text{--}500^\circ\text{C}$ where it was held for 36 h. The doping level of H was controlled by adjusting the processing temperature.

The H-doped NdFeAsO films were photolithographically patterned and Ar-ion-beam-etched to make two kinds of bridges (50 μm wide and 0.5 mm long) as shown in Fig. 1(b). They were used for measuring the transport properties in the longitudinal direction (abbreviated as L bridge) and in the transverse direction (T bridge), respectively [Fig. 1(a)]. A four-probe method was employed with a bias current of 1 μA to measure resistivity using a physical properties measurement system. The onset superconducting transition temperature T_c^{onset} was determined as the intersection between the fit to the normal-state resistivity and the steepest slope of the transition region. The zero resistivity temperature T_c^0 was defined by a resistivity criterion, $\rho_{\text{cri}} = 0.05 \mu\Omega \text{ cm}$, which

corresponds to the noise level of our experimental setup (see the Supplemental Material [21]). In the longitudinal direction, the current flows only in the ab plane, so the longitudinal resistivity ρ_L is the same as the ab -plane resistivity (i.e. $\rho_{ab} = \rho_L$), whereas in the transverse direction, the current flows both in the ab plane and along the c axis. Therefore, ρ_c can be calculated from the transverse resistivity (ρ_T) by the following equation [22]:

$$\rho_c = (\rho_T - \rho_L \cos^2 \alpha) / \sin^2 \alpha. \quad (1)$$

The Hall resistivity ρ_{xy} was measured in the field range of up to $\mu_0 H = \pm 9 \text{ T}$ at 50 K. As expected, the slope corresponding to the Hall coefficient R_H was always negative, indicating that the dominant carriers are electrons. The carrier density n was evaluated using the single carrier model formula,

$$R_H = -\frac{1}{ne}. \quad (2)$$

Here, e is the elementary charge. Note that for the Hall effect measurements, the bias current was supplied along the longitudinal direction, whereas the Hall voltage was measured along the transverse direction, which is the tilted direction. This may lead to a deviation between the actual carrier density and the measured one [23]. The upper critical field H_{c2} was determined by measuring the field dependence of resistivity and using a criterion of 90% of the normal-state resistivity.

III. RESULTS AND DISCUSSION

A. Structural characterization

The specifications of the samples studied here are listed in Table I. For convenience, these samples are named in the order of their carrier densities. We used five as-grown films. Samples B and E were prepared from the same as-grown film, and all other samples were prepared from different as-grown films. As stated above, the doping level of H can be controlled by adjusting the processing temperature T_{proc} . However, this

TABLE I. Sample name, carrier density n , processing temperature T_{proc} of topotactic reaction, the c -axis lattice parameter, the growth angle (offset angle of the sample) α , and the onset T_c (T_c^{onset}) of the samples of this paper. The samples are named in the order of the carrier density for convenience.

Sample name	n ($10^{21}/\text{cm}^3$)	T_{proc} ($^{\circ}\text{C}$)	c axis (\AA)	α ($^{\circ}$)	T_c^{onset} (K)
A	1.51	440	8.482 ± 0.009	5.75	50.5
B	2.28	460	8.418 ± 0.016	5.81	42.1
C	2.75	450	8.418 ± 0.003	4.95	43.1
D	3.99	500	8.424 ± 0.012	6.21	37.4
E	4.23	470	8.386 ± 0.005	5.92	27.8
F	5.03	470	8.361 ± 0.004	5.93	24.3

applies only to the samples derived from the same as-grown film. That is why the correlation between n and T_{proc} seems to be weak (see Table I).

XRD patterns of samples B and E, both originating from the same as-grown film, are compared in Fig. 2. For comparison, the pattern of the as-grown film is also shown. Although small peaks arising from impurities were observed for sample B, the XRD patterns of all samples including those not shown here dominantly consist of the 00 l peaks of the NdFeAs(O,H) phase and the substrate peaks, indicating that they are c -axis oriented. The intensity of the 002 peaks of the doped samples in Fig. 2 were small and almost indistinguishable from the background. Our study using an ordinary (not a vicinal-cut) substrate shows that the intensity of the 002 peak relative to the other peaks decreases with H doping (see the Supplemental Material [21]). Hence, the weaker intensity is, at least partially, due to the slight change in the crystal coordinates and the difference in the atomic scattering factors of oxygen and hydrogen. However, a slight degradation of the crystallinity cannot be ruled out completely. By comparing

the doped samples with the as-grown one, clear shifts of the 00 l peaks to higher angles are recognized, which reflects the reduction in the c -axis length. The evaluated c -axis lengths for all samples are summarized in Table I. The carrier density and the c -axis length are well correlated, which is consistent with our previous results on NdFeAs(O,H) grown on ordinary MgO(001) substrates [18] and found in bulk H-doped or F-doped $Ln\text{FeAsO}$ samples [24,25].

B. Resistivity measurements at zero magnetic field

The temperature dependencies of the resistivity in the transversal and longitudinal directions for all samples are summarized in Fig. 3(a). As can be seen, the transversal resistivity is always larger than the longitudinal one because ρ_T contains the ρ_c component. For all samples, each pair of transversal and longitudinal bridges fabricated from the same film possess the same T_c^{onset} and T_c^0 , proving that the films are chemically homogeneous.

The carrier density dependencies of both T_c^{onset} and T_c^0 are plotted in Fig. 3(b). Both T_c^{onset} and T_c^0 decreased with increasing carrier concentration. As the behavior of T_c^{onset} and T_c^0 on n are similar, T_c^{onset} is regarded as T_c from here on for simplicity.

The temperature dependencies of the in-plane resistivity $\rho_{ab}(T)$ and the out-of-plane resistivity $\rho_c(T)$ of all samples are plotted in Figs. 4(a) and 4(b), respectively. All $\rho_{ab}(T)$ curves exhibited a metallic behavior irrespective of n . However, the shape of the $\rho_{ab}(T)$ curve for samples E and F is obviously different from that of samples A, B, and C. The $\rho_{ab}(T)$ curves of the former samples have a positive curvature, whereas those of the latter samples are slightly negative. On the other hand, sample E shows an almost linear temperature dependence from T_c to 120 K (see the Supplemental Material [21]). This will be discussed later. The behavior of $\rho_c(T)$ shown in Fig. 4(b) is converse to that of $\rho_{ab}(T)$. ρ_c depends almost linearly to temperature at larger n , whereas the $\rho_c(T)$ curves of the less doped samples have a negative curvature. Moreover, the temperature dependence of ρ_c for samples A–C showed a peak at around 250–275 K, which may correspond to a crossover from incoherent conduction at high temperatures to coherent conduction at low temperatures as was observed, for instance, also in the BaFe_2As_2 system [26]. Note that the XRD correlation length L evaluated by the Williamson-Hall analysis is close to the film thickness (20–30 nm) and independent of carrier concentration [27] (see the

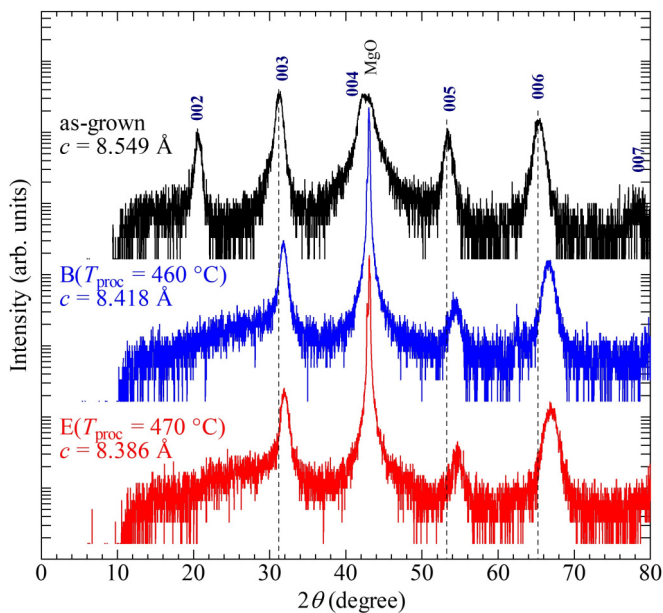


FIG. 2. The $2\theta/\omega$ scans of samples B (blue) and E (red), which were processed at 460 $^{\circ}\text{C}$ and 470 $^{\circ}\text{C}$, respectively. For comparison, the $2\theta/\omega$ scan of the corresponding pristine film (black) without doping is also shown.

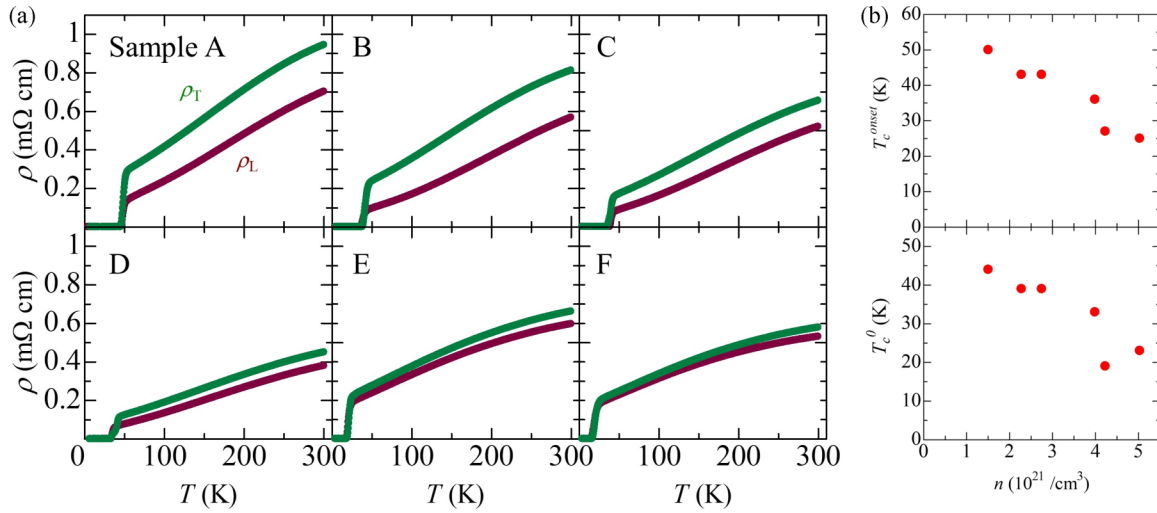


FIG. 3. (a) The temperature dependencies of ρ_L (copper) and ρ_T (green) for samples A–F. (b) T_c^{onset} and T_c^0 as a function of the carrier density for NdFeAs(O,H).

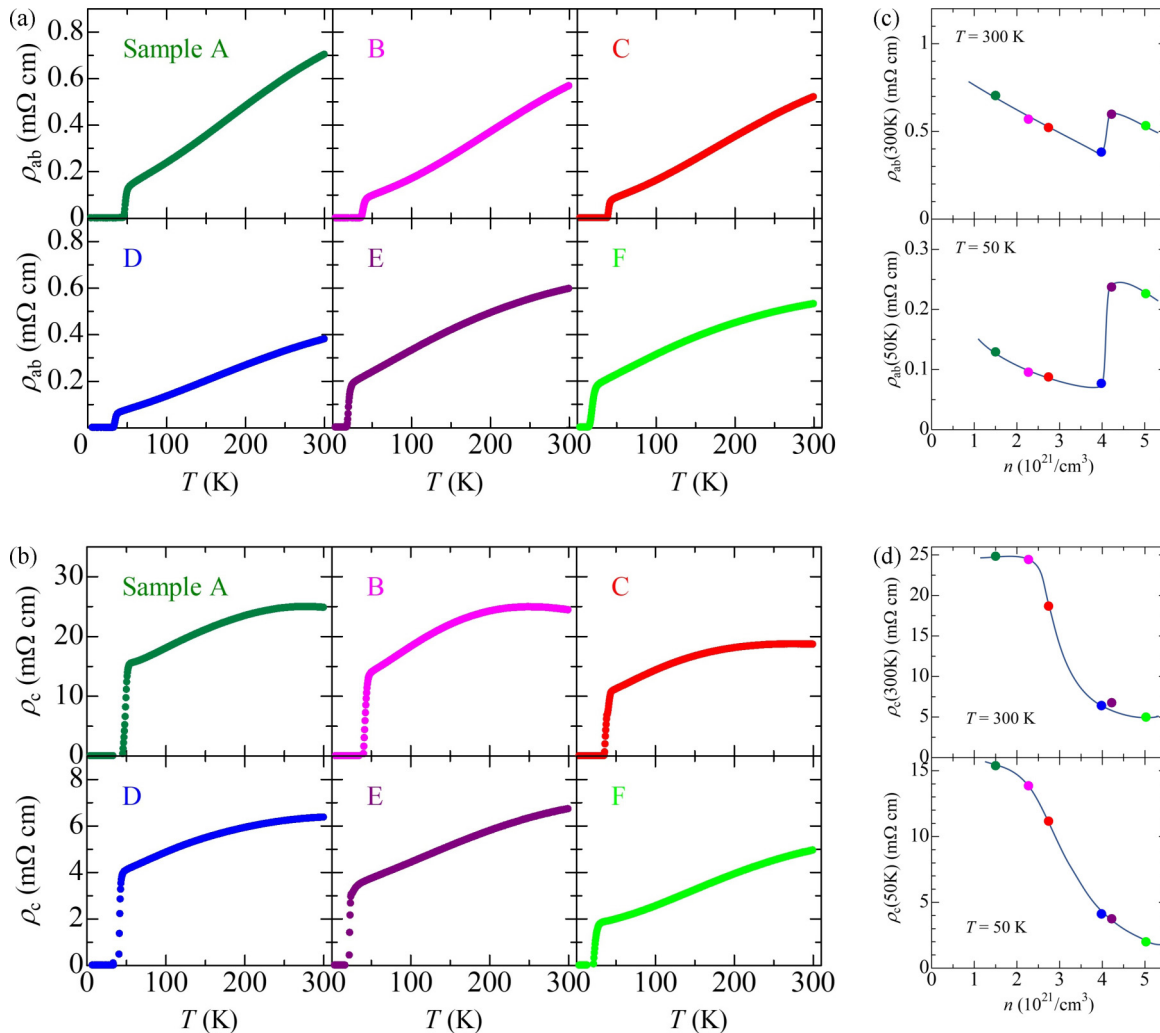


FIG. 4. (a) and (b) The temperature dependence of (a) ρ_{ab} and (b) ρ_c of samples A (green), B (fuchsia), C (red), D (blue), E (copper), and F (lime). (c) and (d) The carrier density dependencies at 300 and 50 K for (c) ρ_{ab} and (d) ρ_c , respectively. For sample A, the resistivities (ρ_{ab} and ρ_c) at 50 K were determined by extrapolating the result of linear regression in the temperature range of $55 \text{ K} < T < 65 \text{ K}$ to $T = 50 \text{ K}$ for its high T_c^{onset} ($=50 \text{ K}$). The solid line is a guide to the eye.

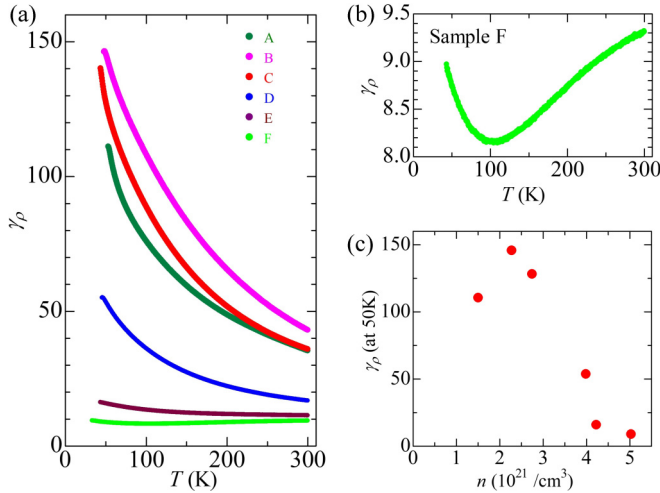


FIG. 5. (a) The temperature dependence of the resistivity anisotropy $\gamma_\rho(T) = \rho_c/\rho_{ab}$ of samples A–F. (b) An enlarged view of $\gamma_\rho(T)$ of sample F. (c) The carrier density dependence of $\gamma_\rho(T)$ of NdFeAs(O,H).

Supplemental Material [21]). Thus, the variation of ρ_c is not due to the change in the microstructure but the H content.

Figure 4(c) shows the n dependence of ρ_{ab} at 300 and 50 K. ρ_{ab} at both 300 and 50 K decrease with increasing n up to $4 \times 10^{21}/\text{cm}^3$. An abrupt rise in ρ_{ab} at around $n = 4 \times 10^{21}/\text{cm}^3$ is observed at both 300 and 50 K. This carrier concentration coincides with that where a quantum critical point (QCP) may be present as will be discussed later. Unlike ρ_{ab} , ρ_c at 300 and 50 K decreases monotonically with increasing n as shown in Fig. 4(d).

The resistivity anisotropy γ_ρ is shown in Fig. 5(a) as a function of temperature. For samples A–E, γ_ρ increases monotonically with decreasing T . This behavior is the same as that of optimally F-doped NdFeAsO thin films [19]. The maximum γ_ρ of the samples with a T_c above 40 K reaches about 100–150 just above T_c . The temperature dependence of γ_ρ becomes weaker, and the value of γ_ρ decreases as n increases. Finally, γ_ρ of the highest-doped sample has a different temperature dependence. It decreases with decreasing temperature and records a minimum of about 8 around 100 K before increasing at lower temperatures as shown in Fig. 5(b). Although the variation in the temperature dependence of the present sample F is small, the minimum of γ_ρ might be an indication of a phase transition at around 100 K. In fact, a structural transition was observed for SmFeAs(O,D) and LaFeAs(O,H) at about 100 K in the overdoped region, where the c -axis length showed a minimum [6,28]. As a shorter c -axis length means an increased connectivity between the FeAs conducting layers, this may explain the minimum of the resistivity anisotropy.

Figure 5(c) shows the carrier density dependence of γ_ρ at 50 K for H-doped NdFeAsO. The films with higher T_c tend to have a larger anisotropy. The peak of γ_ρ is located at around $n = 2.2 \times 10^{21}/\text{cm}^3$, which corresponds to the high- T_c region [see Fig. 3(b)]. It is notable that the optimally F-doped sample has a larger anisotropy than the H-doped samples [19]. This might be explained by the more two-dimensional character of

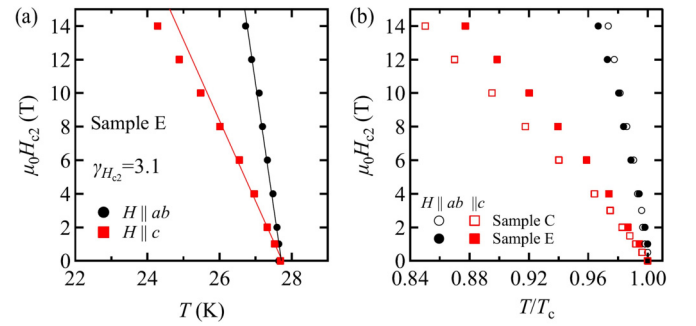


FIG. 6. (a) Temperature dependence of H_{c2} of sample E for $H \parallel ab$ and $\parallel c$. The solid lines show the results of linear fitting to the data up to 8 T. (b) Comparison between samples C and E.

the Fermi surface of F-doped samples [8]. Alternatively, the high reactivity of fluorine may have introduced some damage to the crystal during the fluorination that disturbed the inter-plane conductivity.

C. In-field resistivity measurements of samples C and E

The upper critical fields H_{c2} of sample E determined from the in-field ρ_{ab} measurements for both $H \parallel c$ and $\parallel ab$ are summarized in Fig. 6(a). The respective slopes of the temperature dependence are -4.8 T/K and -14.8 T/K near T_c for $H \parallel c$ and $\parallel ab$, which gives an anisotropy of 3.1. For single-band superconductors, the anisotropy of the upper critical field $\gamma_{H_{c2}} (= H_{c2\perp}/H_{c2\parallel})$, $H_{c2\perp}$ and $H_{c2\parallel}$ are the upper critical fields for $H \parallel ab$ and $\parallel c$ equals $\sqrt{\gamma_\rho}$ ($= \sqrt{\gamma_m}$). This relation does not necessarily hold for multiband superconductors. Nevertheless, the value of $\gamma_{H_{c2}}$ is relatively close to the square root of the resistivity anisotropy [$\gamma_\rho(50 \text{ K}) \sim 15$] of sample E.

We also measured the resistivity under magnetic fields in the flux-flow regime of sample E and found that the angle dependence of resistivity under various magnetic fields collapses to a single curve when plotted as a function of an effective magnetic-field $\mu_0 H_{\text{eff}} = \mu_0 H / f_T(\theta)$, where $f_T(\theta)$ is the Tinkham formula given by [29]

$$f_T(\theta) = \frac{1}{2\gamma_{H_{c2}}^2 \sin^2\theta} \left[\sqrt{\cos^2\theta + \gamma_{H_{c2}}^2 \sin^2\theta} - |\cos\theta| \right]. \quad (3)$$

Here, θ is the angle between the magnetic field and the c axis. Figure 7 shows the data taken at 26.5 K. The anisotropy parameter $\gamma_{H_{c2}}$ was determined as 3.2 ± 0.1 from the scaling of Fig. 7(b), consistent with the value obtained from the temperature slope of H_{c2} . It is also noticeable that the dip in the resistance curve is shifted from 270° to a higher angle at low magnetic fields due to the tilted growth of the film and the corresponding nonparallelity of B and H [see Fig. 7(c)] [30]. The shift of the resistance dip explains the slight deviation of the data near zero effective field from the scaling curve in Fig. 7(b). Resistivity scaling at slightly higher temperatures (27.0 and 27.5 K) with the same value of $\gamma_{H_{c2}}$ were of similar quality. On the assumption that the relaxation time of carriers is isotropic, the resistivity anisotropy is equal to the mass anisotropy. In our previous study, the mass anisotropy was different in the normal and superconducting states for under- and

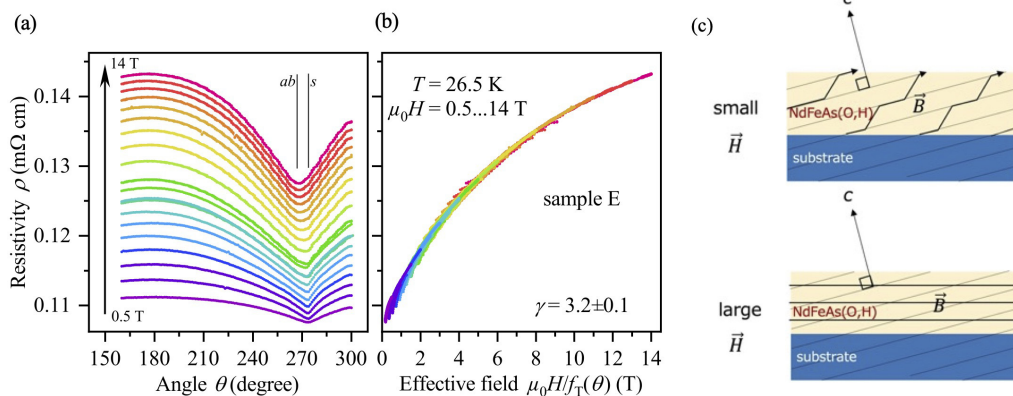


FIG. 7. (a) Angular dependence of the resistivity at 26.5 K. The magnetic fields were increased by 0.5 T up to 5.0 T and by 1.0 T further on. A shift of the resistance dip from $H||ab$ towards the substrate surface direction (s) at low magnetic fields due to nonparallelity of B and H is clearly observed. (b) Two-dimensional (Tinkham) scaling of the data shown in (a). An anisotropy value of $\gamma_{H_{c2}} = 3.2 \pm 0.1$ yielded the best result. (c) Schematics of how the direction of B changes with the strength of the applied magnetic field. When a weak magnetic field is applied parallel to the substrate, B is almost parallel to the crystallographic ab plane due to the trapping of B along the Nd(O,H) blocking layers. On the other hand, as a strong magnetic field is applied, the direction of B is parallel to that of H .

optimally F-doped NdFeAsO [19]. Hence, the rough match of the mass anisotropy in the normal state with the one in the superconducting state may be one of the distinct features of the overdoped side of the phase diagram. Figure 6(b) compares H_{c2} of sample E with that of a less doped one (sample C) as a function of the reduced temperature $t = T/T_c$. For $H||ab$, $H_{c2}(t)$ of both samples is almost identical. On the other hand, for $H||c$, sample E shows a higher H_{c2} at the same reduced temperature T/T_c . This is probably due to an increased coupling between FeAs layers with increasing doping.

D. Exponent of power-law behavior $\rho_{ab}(T) = \rho_0 + AT^\beta$

In order to quantify the behavior of the temperature dependence of ρ_{ab} , we examined the exponent β by assuming $\rho_{ab}(T) = \rho_0 + AT^\beta$ in the temperature range from just above T_c to 120 K, where ρ_0 is the residual resistivity at zero kelvin and A is a constant. The obtained β is plotted against the carrier density in Fig. 8(a), which shows a domelike shape. A

similar behavior was also found for polycrystalline $LnFeAs(O,H)$ [11].

To investigate the exponent β in more detail, we employed the formula $\beta(T) = \frac{d \ln(\rho_{ab} - \rho_0)}{d \ln T}$ to extract the temperature dependence of β over a wide temperature range [Fig. 8(b)] where the ρ_0 value obtained by the fitting described above was used. For all samples, β is close to 2 at the temperature very close to T_c , indicative of a Fermi-liquid state. A similar behavior was also found in $FeSe_{0.89}S_{0.11}$ under various pressures [31]. At higher temperatures, β is smaller than 2. For example, β is almost constant around 1.5 for a wide temperature range from 200 K to close to T_c as shown in Fig. 8(b) for sample B, consistent with the result of the fitting mentioned above.

At $n \cong 4.2 \times 10^{21}/\text{cm}^3$, on the other hand, β was close to 1 over the temperature range from 150 K to T_c , and the general trend of the resistivity curve changed from positive ($\beta > 1$) to negative ($\beta < 1$) curvature with further increasing n . Intriguingly, a rather abrupt change in the ρ_{ab} value was observed at this carrier density as pointed out above [Fig. 4(c)].

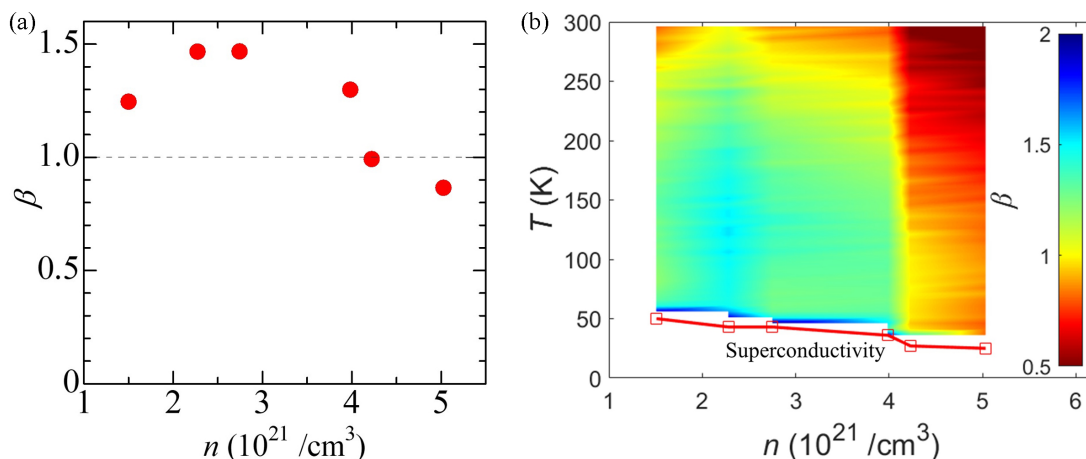


FIG. 8. (a) Relationship between the exponent β and n . The exponent β was obtained by fitting the power-law form $\rho(T) = \rho_0 + AT^\beta$ to the resistivity data in the temperature range of $T_c < T \leq 120$ K. The dashed line indicates $\beta = 1$. (b) The carrier density-temperature phase diagram. The color map represents the exponent β .

The T -linear behavior of resistivity has often been associated with a quantum critical point at $T = 0$ K. However, the T -linear behavior usually extends to a fanlike region around the quantum critical point on the phase diagram [32], although here it is observed only in a striplike region. The electronic phase diagram of H-doped LaFeAsO reported by Hiraishi *et al.* shows that the second antiferromagnetic phase (AFM2) and superconductivity may coexist in the overdoped region [28]. The Néel temperature decreases with the application of a high pressure, and the presence of a pressure-induced quantum critical point (QCP) was suggested from NMR measurements [33]. The anomalous behaviors we have observed at $n \cong 4.2 \times 10^{21}/\text{cm}^3$ might be a glimmering of this QCP at ambient pressure, although whether they are indeed related or not is an open question for future studies. Note though that the actual carrier density might be slightly different as mentioned in the experimental section.

For larger values of n , β is less than 1 in the whole temperature range. For a SmFeAsO_{0.9}H_{0.1} single crystal, an exponent $\beta = 0.47$ was reported and associated with the spin-frozen state that locates between AFM1 and the superconducting phases [15]. The electronic phase diagram of $Ln\text{FeAsO}$ shows that AFM1 and AFM2 exist close to the superconducting phase in the underdoped and the overdoped regimes, respectively [6,28]. It might be possible to explain the small β value in the overdoped region similarly.

IV. CONCLUSION

NdFeAs(O,H) epitaxial thin films with different doping concentrations were grown on vicinal-cut MgO substrates by MBE. With the combination of F-doped samples in the lower carrier density regime, a large part of the phase diagram can be mapped. The temperature dependence of both ρ_{ab} and ρ_c exhibits metallic behavior irrespective of the doping level for all samples studied in this paper. The extracted resistivity anisotropy γ_ρ showed a strong doping dependence. At the H concentrations which led to superconducting transition temperatures (T_c) over 40 K, γ_ρ recorded ~ 100 – 150 at 50 K. With increasing the carrier concentration, γ_ρ eventually reached a remarkably small value around 8. We extracted the T -dependent exponent β of $\rho_{ab}(T)$ and discussed the possible presence of a QCP at the overdoped side of the phase diagram.

ACKNOWLEDGMENTS

This work was supported by JST CREST Grant No. JP-MJCR18J4, JSPS Grant-in-Aid for Scientific Research (B) Grant No. JP20H02681, and Japan-German Research Cooperative Program between JSPS and DAAD, Grant No. JPJSBP120203506.

-
- [1] J. Xu, C. Pan, T. Takata, and K. Domen, *Chem. Commun.* **51**, 7191 (2015).
- [2] F. Takeiri, F. Takeiri, A. Watanabe, A. Kuwabara, H. Nawaz, Nur Ika Puji Ayu, M. Yonemura, R. Kanno, and G. Kobayashi, *Inorg. Chem.* **58**, 4431 (2019).
- [3] Z. A. Ren, W. Lu, and J. Yang, *Chin. Phys. Lett.* **25**, 2215 (2008).
- [4] H. Hiramatsu, T. Katase, T. Kamiya, M. Hirano, and H. Hosono, *Appl. Phys. Lett.* **93**, 162504 (2008).
- [5] T. Hanna, Y. Muraba, S. Matsuishi, N. Igawa, K. Kodama, S. I. Shamoto, and H. Hosono, *Phys. Rev. B* **84**, 024521 (2011).
- [6] S. Iimura, H. Okanishi, S. Matsuishi, H. Hiraka, T. Honda, K. Ikeda, T. C. Hansen, T. Otomo, and H. Hosono, *Proc. Natl. Acad. Sci. USA* **114**, E4354 (2017).
- [7] M. Fujioka, S. J. Denholme, T. Ozaki, H. Okazaki, K. Deguchi, S. Demura, H. Hara, T. Watanabe, H. Takeya, and T. Yamaguchi, *Supercond. Sci. Technol.* **26**, 085023 (2013).
- [8] Y. Muraba, S. Matsuishi, and H. Hosono, *Phys. Rev. B* **89**, 094501 (2014).
- [9] N. Xu, T. Qian, P. Richard, Y.-B. Shi, X.-P. Wang, P. Zhang, Y.-B. Huang, Y.-M. Xu, H. Miao, G. Xu, G.-F. Xuan, W.-H. Jiao, Z.-A. Xu, G.-H. Cao, and H. Ding, *Phys. Rev. B* **86**, 064505 (2012).
- [10] K. Iida, V. Grinenko, F. Kurth, A. Ichinose, I. Tsukada, E. Ahrens, A. Pukenas, P. Chekhonin, W. Skrotzki, A. Teresiak, R. Hühne, S. Aswartham, S. Wurmehl, I. Mönch, M. Erbe, J. Hänisch, B. Holzapfel, S. Drechsler, and D. V. Efremov, *Sci. Rep.* **6**, 28390 (2016).
- [11] S. Iimura, S. Matsuishi, H. Sato, T. Hanna, Y. Muraba, S. W. Kim, J. E. Kim, M. Takata, and H. Hosono, *Nat. Commun.* **3**, 943 (2012).
- [12] H. Kashiwaya, K. Shirai, T. Matsumoto, H. Shibata, H. Kambara, M. Ishikado, H. Eisaki, A. Iyo, S. Shamoto, I. Kurosawa, and S. Kashiwaya, *Appl. Phys. Lett.* **96**, 202504 (2010).
- [13] P. J. W. Moll, R. Puzniak, F. Balakirev, K. Rogacki, J. Karpinski, N. D. Zhigadlo, and B. Batlogg, *Nature Mater.* **9**, 628 (2010).
- [14] M. Fujioka, S. J. Denholme, M. Tanaka, H. Takeya, T. Yamaguchi, and Y. Takano, *Appl. Phys. Lett.* **105**, 102602 (2014).
- [15] S. Iimura, T. Muramoto, S. Fujitsu, S. Matsuishi, and H. Hosono, *Asian Ceram. Soc.* **5**, 357 (2017).
- [16] J. Matsumoto, K. Hanzawa, M. Sasase, S. Haindl, T. Katase, H. Hiramatsu, and H. Hosono, *Phys. Rev. Mater.* **3**, 103401 (2019).
- [17] H. Hiramatsu, J. Matsumoto, and H. Hosono, *Appl. Phys. Express* **13**, 073002 (2020).
- [18] K. Kondo, S. Motoki, T. Hatano, T. Urata, K. Iida, and H. Ikuta, *Supercond. Sci. Technol.* **33**, 09LT01 (2020).
- [19] K. Iida, T. Matsumoto, K. Kondo, T. Hatano, and H. Ikuta, *Supercond. Sci. Technol.* **33**, 044016 (2020).
- [20] T. Kawaguchi, H. Uemura, T. Ohno, M. Tabuchi, T. Ujihara, Y. Takeda, and H. Ikuta, *Appl. Phys. Express* **4**, 083102 (2011).
- [21] See Supplemental Material at <http://link.aps.org/supplemental/10.1103/PhysRevMaterials.6.054802> where we describe (i) determination of the onset superconducting transition temperature T_c^{onset} and zero resistance temperature T_c^0 , (ii) $2\theta/\omega$ scans of NdFeAs(O,H) films grown on CaF₂ substrates, (iii) resistivity curves $\rho_{ab}(T)$, and (iv) Williamson-Hall plot for analyzing the correlation length.
- [22] T. Zahner, R. Stierstorfer, R. Rössler, J. D. Pedarnig, D. Bäuerle, and H. Lengfellner, *Physica C* **298**, 91 (1998).

- [23] G. Heine, W. Lang, R. Rössler, and J. D. Pedarnig, *Nanomaterials* **11**, 675 (2021).
- [24] S. Matsuishi, T. Hanna, Y. Muraba, S. W. Kim, J. E. Kim, M. Takata, S. I. Shamoto, R. I. Smith, and H. Hosono, *Phys. Rev. B* **85**, 014514 (2012).
- [25] F. Shahbaz Tehrani and V. Daadmehr, *J. Supercond. Nov. Magn.* **33**, 337 (2020).
- [26] M. Nakajima, M. Nagafuchi, and S. Tajima, *Phys. Rev. B* **97**, 094511 (2018).
- [27] H-M. Wang, J-P. Zhang, C-Q. Chen, Q. Fareed, J-W. Yang, and M. Asif Khan, *Appl. Phys. Lett.* **81**, 604 (2002).
- [28] M. Hiraishi, S. Iimura, K. M. Kojima, J. Yamaura, H. Hiraka, K. Ikeda, P. Miao, Y. Ishikawa, S. Torii, M. Miyazaki, I. Yamauchi, A. Koda, K. Ishii, M. Yoshida, J. Mizuki, R. Kadono, R. Kumai, T. Kamiyama, T. Otomo, Y. Murakami, S. Matsuishi, and H. Hosono, *Nat. Phys.* **10**, 300 (2014).
- [29] R. Fastampa, S. Sarti, E. Silva, and E. Milani, *Phys. Rev. B* **49**, 15959 (1994).
- [30] A. V. Silhanek, L. Civale, and M. A. Avila, *Phys. Rev. B* **65**, 174525 (2002).
- [31] P. Reiss, D. Graf, A. A. Haghighirad, W. Knafo, L. Drigo, M. Bristow, A. J. Schofield, and A. I. Coldea, *Nat. Phys.* **16**, 89 (2020).
- [32] H. v. Löhneysen, A. Rosch, M. Vojta, and P. Wölfle, *Rev. Mod. Phys.* **79**, 1015 (2007).
- [33] M. Takeuchi, N. Fujiwara, T. Kuwayama, S. Nakagawa, S. Iimura, S. Matsuishi, Y. Yamakawa, H. Kontani, and H. Hosono, *Phys. Rev. B* **99**, 174517 (2019).